The Astrophysical Journal, 627:140–155, 2005 July 1

THE X-RAY EMISSIONS FROM THE M87 JET: DIAGNOSTICS AND PHYSICAL INTERPRETATION

Eric S. Perlman[1,2] and Andrew S. Wilson[3,4]
Received 2004 October 22; accepted 2005 March 2

ABSTRACT

We reanalyze the deep *Chandra* observations of the M87 jet, first examined by Wilson & Yang in 2002. By employing an analysis chain that also includes image deconvolution, knots HST-1 and I are fully separated from adjacent emission. We derive the spatially resolved X-ray spectrum of the jet using the most recent response functions and find slight but significant variations in the spectral shape, with values of $\alpha_X(S_\nu \propto \nu^{-\alpha})$ ranging from $\sim$1.2–1.4 (in the nucleus and knots HST-1, D, and C) to $\sim$1.6 (in knots F, A, and B). We make use of VLA radio observations, as well as *HST* imaging and polarimetry data, to examine the jet's broadband spectrum and inquire as to the nature of particle acceleration in the jet. As shown in previous papers, a simple continuous injection model for the synchrotron-emitting knots, in which one holds constant both the filling factor f_{acc} of the regions within which particles are accelerated and the energy spectrum of the injected particles, cannot account for the flux or spectrum of the X-ray emission. Instead, we propose that f_{acc} is a function of both position and energy and find that in the inner jet, $f_{acc} \propto E_\gamma^{-0.4\pm0.2} \propto E_e^{-0.2\pm0.1}$, and in knots A and B, $f_{acc} \propto E_\gamma^{-0.7\pm0.2} \propto E_e^{-0.35\pm0.1}$, where E_γ is the energy of the emitted photon and E_e is the energy of the emitting electron. In this model, the index p of the relativistic electron energy spectrum at injection $[n(E_e) \propto E_e^{-p}]$ is $p = 2.2$ at all energies and all locations along the jet, in excellent agreement with the predictions of models of cosmic-ray acceleration by ultrarelativistic shocks ($p = 2.23$). There is a strong correlation between the peaks of X-ray emission and minima of optical percentage polarization, i.e., regions where the jet magnetic field is not ordered. We suggest that the X-ray peaks coincide with shock waves that accelerate the X-ray–emitting electrons and cause changes in the direction of the magnetic field; the polarization is thus small because of beam averaging.

Subject headings: galaxies: active — galaxies: individual (M87) — galaxies: jets — galaxies: nuclei — magnetic fields — X-rays: galaxies

1. INTRODUCTION

The giant elliptical galaxy M87 hosts the best-known extragalactic jet. As a result of its proximity (distance = 16 Mpc [Tonry 1991], for a scale of $1'' = 78$ pc) and high surface brightness from radio through X-rays, particularly high resolution studies of its structure are possible. The synchrotron nature of the jet's optical emissions was first demonstrated by Baade (1956), who found it to be highly polarized. The first high-quality imaging polarimetry and photometry was done in the 1970s, in both the radio (De Young et al. 1979) and optical (Schmidt et al. 1978). Those observations showed a magnetic field predominantly parallel to the local jet direction, highlighting the importance of an understanding of the field structure. Subsequent observations in the radio (Owen et al. 1989 and references therein; Biretta et al. 1995; Zhou 1998), mid-IR (Perlman et al. 2001b), and near-IR/optical (Meisenheimer et al. 1996; Sparks et al. 1996; Perlman et al. 1999, 2001a, hereafter P99, P01a) have featured detailed studies of the jet's structure, allowing models of synchrotron emission to be fit to the broadband spectrum of each knot in the jet, and also allowing the axial and magnetic field structure to be probed.

Given its high surface brightness, it is not surprising that the jet of M87 was also one of the first three jets detected in the X-ray band by *Einstein* (Schreier et al. 1981; Biretta et al. 1991), along with those of Cen A (Schreier et al. 1979; Feigelson et al. 1981) and 3C 273 (Harris & Stern 1987). However, prior to the launch of *Chandra* in 1999, very little was known about its X-ray structure. X-ray emission had been discovered from three of the knots in the jet by Biretta et al. (1991), but due to the low angular resolution of the *Einstein* and *ROSAT* data ($\gtrsim 5''$, compared to jet features that are $\sim 1''$ in extent), it was not possible to make detailed analyses of the jet's X-ray morphology, let alone comparisons to the radio or optical.

Chandra observations of the M87 jet have revealed X-ray emissions from every knot in the M87 jet (Marshall et al. 2002, hereafter M02; Wilson & Yang 2002, hereafter WY02). The X-ray spectra of the knots are steeper than those in the radio and optical bands, confirming that the X-ray emission is not inverse Compton scattering, for which the same spectral index is expected for the synchrotron and inverse Compton emission from the same electron population. M02 and WY02 argued that the X-ray emission represents the high-energy tail of the synchrotron spectrum. However, the images show intriguing differences between the X-ray morphology of the M87 jet and its morphology in the optical and radio; in particular, the X-ray emissions from some knots appear to be upstream of their optical emissions and, in addition, two X-ray–bright regions (labeled "D-X" and "G" by M02) are seen, which do not coincide with optically bright regions of the jet. By contrast, the radio and optical morphologies of the M87 jet differ only subtly, being quite similar on arcsecond scales but somewhat narrower and "knottier" in the optical, as revealed by the *Hubble Space Telescope* (*HST*) observations (Sparks et al. 1996).

X-ray synchrotron emitting electrons have $\gamma = E/mc^2 \sim 10^7 - 10^8$ and radiative lifetimes of a few to tens of years (given

[1] Department of Physics, Joint Center for Astrophysics, University of Maryland–Baltimore County, 1000 Hilltop Circle, Baltimore, MD 21250; perlman@jca.umbc.edu.
[2] Department of Physics and Astronomy, Johns Hopkins University, 3400 North Charles Street, Baltimore, MD 21218.
[3] Astronomy Department, University of Maryland, College Park, MD 20742; wilson@astro.umd.edu.
[4] Space Telescope Science Institute, 3700 San Martin Drive, Baltimore, MD 21218.

the magnetic field strengths estimated by Meisenheimer et al. 1996 or Heinz & Begelman 1997), thus requiring local particle acceleration. Therefore, *Chandra* images of M87 give us the opportunity to probe directly the acceleration of the high-energy particles whose emissions we see. In light of this fact, we decided to analyze together the deepest published *Chandra* image of the M87 jet (WY02) and the multiwaveband Very Large Array (VLA) and *HST* imaging and polarimetry published by P99 and P01a. The goal of this work is to improve our understanding of the physics of the M87 jet and the relationship between the X-ray and optical emissions.

In § 2 we review the observations used in each band. In § 3 we discuss the radio, optical, and X-ray morphology and spectrum of the jet. This discussion includes a presentation of deconvolved images made from the *Chandra X-Ray Observatory* data and a comparison with *HST* images. The deconvolution results in a significant gain in resolution that proves quite helpful in understanding several structural details. We also present in § 3 a detailed discussion of the jet's X-ray and optical–to–X-ray spectrum, including the first optical–to–X-ray spectral index map, as well as a comparison between the jet's X-ray structure and polarized optical emissions. In § 4 we discuss the physical implications of our results, including a model of particle acceleration and insights into the jet structure and magnetic field configuration in the M87 jet. We conclude our discussion in § 5 with a summary.

2. OBSERVATIONS

The data used in this paper have already been discussed by previous authors: the *Chandra* data by WY02, and the VLA and *HST* data by P99 and P01a (see also Zhou 1998 for more details on the VLA observations). In this section, we review the essentials of each data set. For specific information on data reduction procedures (except those noted below, which are specific to this paper) or observational details, we refer the reader to those papers.

2.1. *Chandra Observations*

The *Chandra* data cover the energy range 0.2–10 keV, corresponding to frequencies between 4.8×10^{16} and 2.4×10^{18} Hz. The *Chandra* observations were taken on 2000 July 29–30, using the ACIS-S instrument, with the entire jet on chip S3. The observations were split into two parts after a preliminary 1 ks observation showed that at least three components in M87's X-ray structure would be piled up in a normal 3.2 s frame time observation. A 0.4 s frame time observation with a standard 1/8 subarray was used to obtain accurate spectra and photometry of the brightest components, while a 3.2 s frame time observation using the full S3 CCD (as well as CCDs I2, I3, S1, S2, and S4) allowed fainter structure to be observed (WY02). The good-exposure time of the 0.4 s frame time observation was 12.8 ks, while the 3.2 s frame time data included 37.6 ks of good-exposure time.

For data reduction, we followed the procedures recommended in the CIAO science threads. The data were filtered to exclude times of high background and aspect errors, of which very few were found. Prior to analyzing the *Chandra* data, we resampled the images by a factor of 4, obtaining a scale of $0\farcs123$ pixel^{-1}. We also applied pixel derandomization to the imaging data. Upon examination of the 3.2 s frame time data, four components were found to be piled up: the nucleus as well as knots HST-1, D, and A in the jet (WY02). For these components, it was therefore necessary to use the 0.4 s frame time observations for all analyses. For all other regions of the jet, however, we were able to make use of the higher sensitivity 3.2 s frame time data. All data selection for X-ray spectral analysis was done in CIAO versions 2.2 and 2.3, following the appropriate threads. We included the application of ACISABS to the ARF, which corrects for absorption by contaminants on the surface of the CCD or a pre-CCD filter. For all jet regions, we used X-ray background data selected from $25'' \times 3''$ rectangular regions situated $5''$ north and south of the jet.

For the purposes of analyzing the imaging data, we made use of a hybrid strategy, screening the images to select only the 0.4 s frame time data for pixels within $1\farcs5$ of the centroids of the knots that are piled up in the 3.2 s frame time data, while using a weighted average of the 3.2 and 0.4 s frame time data sets in all other regions. In this way we were able to make an X-ray map of the jet that is essentially unaffected by pileup. A short IDL program was used to do the data selection described above. Using this data selection method, maps were made in the 0.3–1.0, 1–3, and 3–10 keV bands, as well as in the 0.3–1.5 keV (see below) and total bands. These maps were then registered to the VLA data by assuming that the nuclear emission peak is located at the same place in both bands.

To analyze the jet's subarcsecond morphology, we attempted to deconvolve the point-spread function (PSF) from the *Chandra* image. This is a difficult task, since the PSF of *Chandra* is known to be energy-dependent (e.g., Karovska et al. 2001). Fortunately, the energy-dependent variations in the PSF size can be minimized by choosing for deconvolution only X-ray photons with energies between 0.3 and 1.5 keV. At higher energies the PSF has stronger wings due to scattering by the mirror, and the intensity of these wings is energy-dependent. We therefore obtained a 0.3–1.5 keV image, using the data selection described above, and attempted deconvolution using a monochromatic, 1 keV PSF, following the recipe in the "Create a PSF" CIAO 2.2 thread. Several deconvolution algorithms were tried, both in AIPS and IRAF. The most satisfactory results were obtained with the maximum entropy algorithm `vtess` in AIPS. Other algorithms, including the tasks `lucy` in IRAF and `imagr` in AIPS, gave similar results in terms of the source structure but had less even and/or higher noise levels across the image. To reach a stable solution required 150 iterations of `vtess`. Following the application of `vtess`, we smoothed the data with a Gaussian of FWHM $0\farcs2$.

2.2. *HST Observations*

The *HST* images that we discuss in this paper include both multiband imaging and polarimetry. The *HST* data cover the frequency range $(1.5-10) \times 10^{14}$ Hz.

The multiband *HST* imaging data (P01a) were obtained in 1998 with the WFPC2 and NICMOS instruments. Data were obtained on February 25 and 26 through six filters, spanning the wavelength range 0.3–1.6 μm. A seventh near-IR band (2.05 μm) was also scheduled for February 26 but had to be reobserved on 1998 April 4, due to a loss of guide-star lock. Because of the relatively small field of view of the *HST* instruments, we performed the 1998 February observations with the *HST* oriented such that the jet fell along a chip diagonal. Unfortunately, an equally good orientation was not available on April 4; as a result, the F205W data do not include the region within $1''$ of the nucleus. In the F110W and F160W bands, the small size of the NIC1 detector made it necessary to observe at two positions. Most of the observing time for those bands was used on the inner jet (i.e., features interior to knot A, at a distance from the nucleus of $r = 12\farcs4$) because it has a lower optical surface

brightness than the main features of the outer jet (i.e., beyond knot A).

Optical polarimetry of the M87 jet (P99) was obtained on 1995 May 27 with the *HST*, using WFPC2 and the F555W (broadband V) filter plus the POLQ polarization quad filter. In order to maximize the unvignetted field of view available for these observations, we used the WF chips, rather than the PC, for the polarization observations. This is important for the M87 jet, which is over 20″ long; by comparison, the unvignetted field of view on the PC chip using the POLQ filter is only 15″ square, and while most, if not all, of the jet could be included on the unvignetted part of the PC, it would be difficult if not impossible to obtain in this way the good subtraction of the galaxy emission that is critical for polarimetry. Using each of the WF chips with POLQ is equivalent to obtaining images at P.A. $=$ $45^\circ - V3$, $90^\circ - V3$, and $135^\circ - V3$, where $V3$ is the rotation of the HST's z-axis with respect to the sky (for details, see Biretta & McMaster 1997). A total of 1800 s of integration time, split in three to reject cosmic rays, was obtained on each WF chip.

Each *HST* data set was reduced in IRAF using the best recommended flat fields, biases, darks, and illumination correction images. Combination of the *HST* WFPC2 data was done in `crreject` to eliminate cosmic rays. The F814W images, as well as all NICMOS images, were combined using the tasks in the DRIZZLE package. The best available geometrical correction files were used to make minor geometric corrections essential to registering the *HST* data to the radio and X-ray frames of reference. Prior to analyzing the emissions of the jet, we subtracted the galaxy emission, using the tasks `ellipse`, `bmodel`, and `imcalc`. All flux calibration was done using `synphot` in IRAF. As described in P99 and P01a, we registered all *HST* data to the VLA data by assuming that the radio and optical core positions are identical (i.e., the same method as used for the *Chandra* data). In comparing the morphology and spectral properties of the jet in the optical to those in the X-rays, we smoothed the data with Gaussians to 0.″5 resolution to ensure that no effects were present from observing with different resolutions. The polarimetry data were, however, left at the original resolution of 0.″2 to give additional insights into the physics. For more details, we refer the reader to P99 and P01a.

2.3. *VLA Data*

To analyze the jet's broadband spectrum, we also include previously published radio data (Zhou 1998; P99) obtained in 1994 February at 15 GHz. The data reduction procedures for this data set have been described in Zhou (1998) and P99. To facilitate direct comparison between the radio and optical images, the radio image was resampled to the same pixel scale as the *HST* and *Chandra* images. As the absolute astrometry from VLA data is of much higher quality than that which can be attained from either *HST* or *Chandra* data, the position of the nucleus of M87 in the VLA data was used as the absolute astrometric standard (see previous sections).

While the radio data were obtained in 1994 February, the likely effects of variability are small. Even for the largest radio variability found between 1993 and 1997 ($\sim$40% for HST-1; Zhou 1998), the effect on $\alpha_{\rm ro}$ is only $\Delta\alpha_{\rm ro} = 0.04$. As with the *HST* data, we have convolved the VLA data with a Gaussian to obtain 0.″5 resolution.

3. THE MORPHOLOGY AND SPECTRUM OF THE M87 JET

Here we compare the best available images and spectra of the jet at radio, optical, and X-ray frequencies. Below, we first discuss the jet's X-ray morphology and its relationship to the optical and radio morphology (§ 3.1), then its optical–to–X-ray spectral morphology (§ 3.2), and then a comparison of its optical polarimetry and X-ray morphology (§ 3.3).

3.1. *Radio, Optical, and X-Ray Morphology in Total Flux*

In Figure 1 we compare radio, optical, and X-ray images of the M87 jet with images of the radio–optical, optical, and optical–to–X-ray spectral indices ($\alpha_{\rm ro}$, α_o, and $\alpha_{\rm ox}$, respectively). For the purpose of display, all images in Figure 1 were rotated so that the jet is along the x-axis. Also noted in Figure 1 are the historical names for regions in the M87 jet, as in P01a and earlier papers. The X-ray image shown in Figure 1 is that produced using the deconvolution procedure described in § 2.1. As already noted in WY02, the *Chandra* image shows X-ray emission from every knot in the jet, as well as from interknot regions. We attempted to improve the signal-to-noise ratio in faint regions by applying adaptive smoothing; however, the improvement was modest at best, so we do not show that version of the image.

The subarcsecond resolution of *Chandra* is readily apparent in Figure 1; the nucleus has a FWHM of 0.″54 (perpendicular to the jet direction) in the deconvolved image, compared to 0.″84 before deconvolution. Thus the maximum entropy deconvolution that we applied to these data improved the angular resolution by $\approx$35%. This has an immediate effect on our ability to separate important regions of the jet. For example, unlike the undeconvolved images presented in WY02 and M02, here we fully separate the nucleus from HST-1, an X-ray and optically bright knot located only 0.″9 from the nucleus. Similarly, we separate more clearly knots I and A, which are 1″ apart and were not well resolved in undeconvolved images.

The improved resolution also allows us to make out several features that were not immediately apparent in the figures presented by WY02 and M02. Knot D is seen to have significant X-ray structure downstream of its peak; in particular, there does appear to be an X-ray flux enhancement corresponding to the radio/optical feature known as D-W. Figure 1 also shows that there is indeed a weak optical peak associated with the feature called D-X by M02, which was also noted but not named by WY02. Comparison with the optical image reveals that this feature is most likely associated with the upstream end of the knot E region, as its optical and radio counterpart is connected to knot E's optical and radio maxima by an apparent thin bridge. Another feature is apparent further downstream, in knot B1, where the X-ray–bright region appears to be associated with only one of the two apparently crossing filaments seen in the optical and radio (compare with Fig. 1 of P99).

In Figure 2 we plot the profiles of various jet components in the direction perpendicular to the jet, in the radio, optical, and X-rays. In each panel, we also plot, for comparison, the profile of the *Chandra* PSF, represented by that of the nucleus, which is assumed to be unresolved. The profiles in Figure 2 were made by extracting slices 7 pixels (0.″86) wide at the centroid of the named jet component (see Table 1). Three things are apparent from Figure 2. First, it is clear that we do resolve in the transverse direction several regions in the jet with *Chandra*. In particular, the transverse X-ray profiles of knots A, B, and C are wider than the PSF at high significance. There are also indications that the X-ray profiles of knots I and E and possibly knots D-X, D-W, and D-E may be resolved in the transverse direction. The latter results should be verified with deeper imaging data. Second, in the regions where we clearly resolve the X-ray emission, the X-ray flux profile is narrower than that

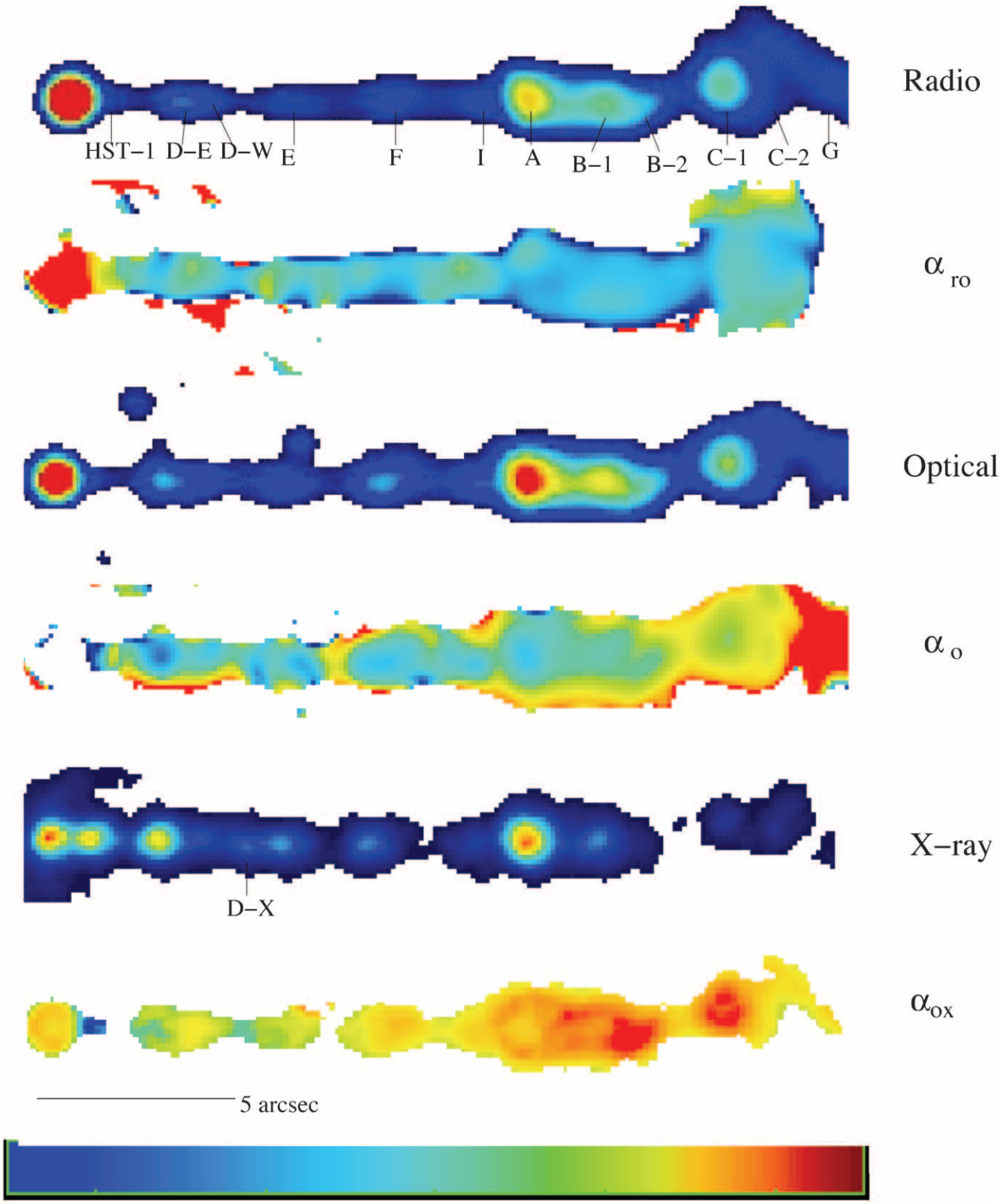

FIG. 1.—Images of the M87 jet. *Top*: Radio (VLA 15 GHz). *Second*: Radio–optical spectral index. *Third*: Optical (*HST* F814W). *Fourth*: Optical spectral index. *Fifth*: X-rays (*Chandra* 0.3–1.5 keV). *Sixth*: Optical–X-ray spectral index. The *Chandra* image has been processed so that pileup is unimportant, and deconvolved using AIPS `vtess` as described in § 2.1, and galaxy light has been subtracted from the optical image as described in P01a. The radio and optical images and spectral index maps were smoothed with Gaussians to a resolution of 0.″5 to match the FWHM of the PSF-deconvolved *Chandra* image (see §§ 2 and 3). The color scales of the spectral index images are as follows: α_{ro}, 0.85 (*red*) to 0.6 (*blue*); α_o, 1.5 (*red*) to 0.4 (*blue*); and α_{ox}, 1.6 (*red*) to 0.9 (*blue*). All images and maps have been rotated so that the jet, which is at P.A. $= -69.^{\circ}5$ (north through east) is along the *x*-axis. The optical image suffers from saturation at the nucleus. The images have been registered by aligning the images of the nuclei, which can be seen at far left. See § 3 for discussion.

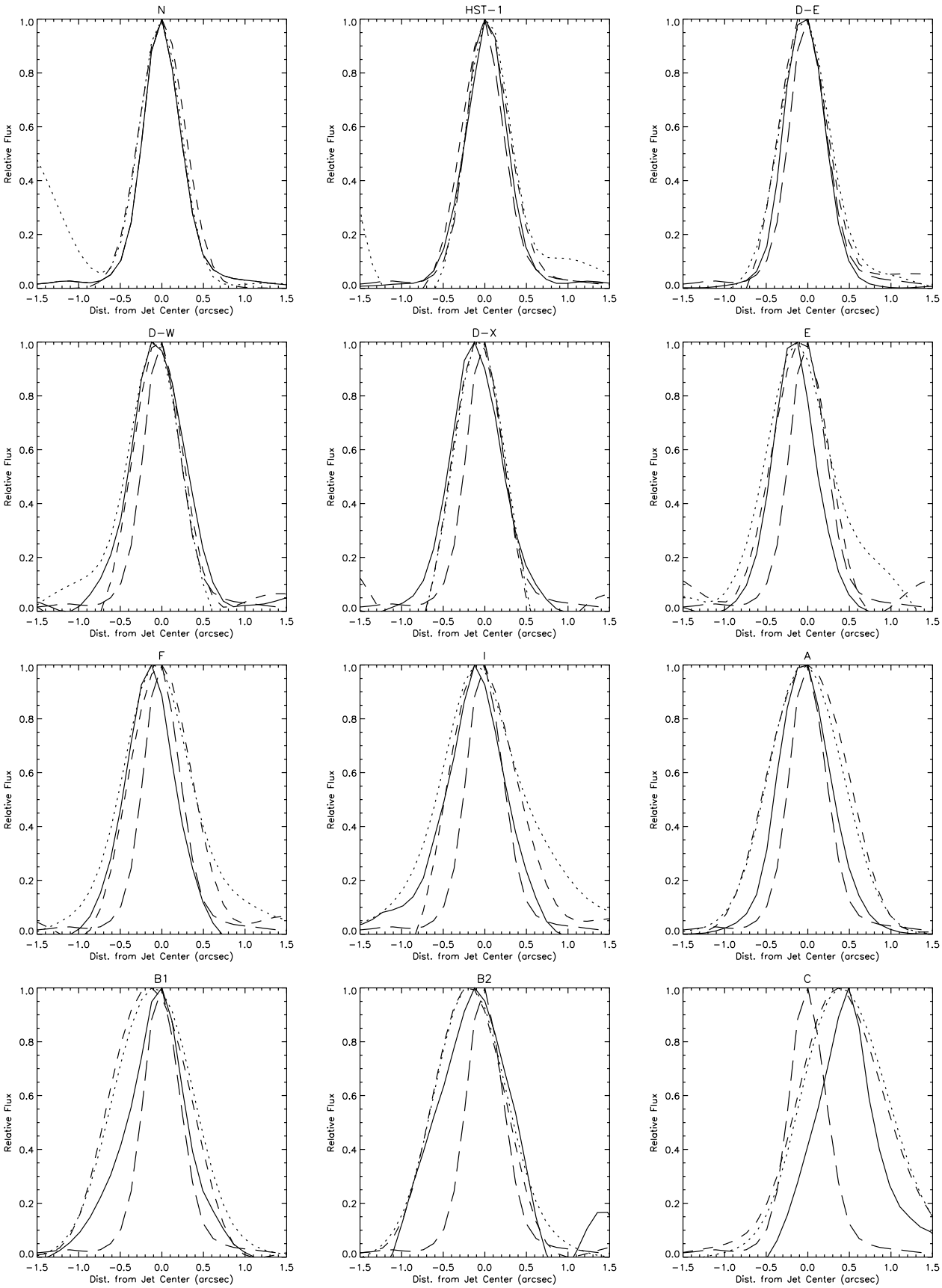

FIG. 2.—Plots of the profile of various jet components in the direction perpendicular to the jet, in the X-ray (*solid line*), radio (*dotted line*), and optical (*dashed line*). For comparison, in each panel (except for the one for the nucleus) we have plotted the *Chandra* PSF, as represented by the profile of the nucleus (*long-dashed line*). All panels are centered at the jet center line, so that the shifts seen represent real offsets north (positive values) or south of the jet center line. Knots A, B, and C are clearly resolved in the *Chandra* data, in the direction perpendicular to the jet. A few other regions are possibly resolved; however, we do not resolve most of the inner jet components. See § 3.1 for discussion.

TABLE 1

X-Ray Positions and Sizes of Jet Components

Component (1)	X-Ray Position (J2000.0) R.A. (2)	X-Ray Position (J2000.0) Decl. (3)	Component Size (FWHM) (arcsec) Major (4)	Component Size (FWHM) (arcsec) Minor (5)	Distance from Nucleus (r) (arcsec) (6)	Optical Position (J2000.0) R.A. (7)	Optical Position (J2000.0) Decl. (8)	ΔR.A. (arcsec) (9)	ΔDecl. (arcsec) (10)	Notes (11)
Nucleus	12 30 49.417 ± 0.001	12 23 28.02 ± 0.01	0.70 ± 0.04	0.58 ± 0.03	0.0	12 30 49.417 ± 0.002	12 23 28.02 ± 0.02	0.0	0.0	a
HST-1	12 30 49.355 ± 0.002	12 23 28.32 ± 0.02	0.79 ± 0.06	0.60 ± 0.04	0.96 ± 0.04	12 30 49.363 ± 0.001	12 23 28.42 ± 0.01	+0.12 ± 0.03	+0.11 ± 0.03	b
D-E	12 30 49.239 ± 0.002	12 23 28.92 ± 0.02	0.85 ± 0.06	0.73 ± 0.05	2.77 ± 0.04	12 30 49.233 ± 0.002	12 23 29.00 ± 0.02	−0.08 ± 0.03	+0.08 ± 0.03	
D-W	12 30 49.165 ± 0.003	12 23 29.34 ± 0.04	0.49 ± 0.0	0.49 ± 0.0	3.92 ± 0.06	12 30 49.188 ± 0.005	12 23 29.18 ± 0.05	+0.33 ± 0.06	−0.16 ± 0.06	c
D-X	12 30 49.089 ± 0.003	12 23 29.61 ± 0.04	0.49 ± 0.0	0.49 ± 0.0	5.05 ± 0.06	12 30 49.070 ± 0.003	12 23 29.82 ± 0.04	−0.27 ± 0.06	+0.21 ± 0.06	c, d
E	12 30 49.030 ± 0.002	12 23 29.94 ± 0.03	1.4 ± 0.2	0.9 ± 0.1	6.00 ± 0.05	12 30 49.017 ± 0.006	12 23 30.10 ± 0.06	−0.18 ± 0.07	+0.16 ± 0.07	d
F	12 30 48.884 ± 0.002	12 23 30.74 ± 0.03	1.6 ± 0.2	1.2 ± 0.2	8.27 ± 0.05	12 30 48.862 ± 0.003	12 23 31.00 ± 0.03	−0.32 ± 0.05	−0.26 ± 0.05	d
I	12 30 48.709 ± 0.004	12 23 31.74 ± 0.05	0.49 ± 0.0	0.49 ± 0.0	11.03 ± 0.08	12 30 48.703 ± 0.001	12 23 31.82 ± 0.01	−0.08 ± 0.05	+0.08 ± 0.05	c, d
A	12 30 48.621 ± 0.001	12 23 32.29 ± 0.02	0.98 ± 0.04	0.91 ± 0.04	12.43 ± 0.03	12 30 48.616 ± 0.001	12 23 32.41 ± 0.01	−0.07 ± 0.02	+0.11 ± 0.02	
B	12 30 48.505 ± 0.006	12 23 32.87 ± 0.07	1.7 ± 0.2	1.3 ± 0.2	14.2 ± 0.1	12 30 48.495 ± 0.001	12 23 32.99 ± 0.01	−0.14 ± 0.08	+0.13 ± 0.08	
C-1	12 30 48.302 ± 0.005	12 23 34.56 ± 0.07	0.49 ± 0.0	0.49 ± 0.0	17.6 ± 0.1	12 30 48.296 ± 0.001	12 23 34.64 ± 0.02	−0.09 ± 0.07	0.09 ± 0.07	c
C-2	12 30 48.211 ± 0.004	12 23 34.94 ± 0.06	0.49 ± 0.0	0.49 ± 0.0	18.98 ± 0.09	12 30 48.256 ± 0.001	12 23 34.68 ± 0.01	+0.66 ± 0.07	−0.25 ± 0.07	

Note.—Units of right ascension are hours, minutes, and seconds, and units of declination are degrees, arcminutes, and arcseconds. Col. (1): Component name. Cols. (2) and (3): Right ascension and declination, as derived from the *Chandra* X-ray data, after assuming the VLA position for the nucleus. Col. (4): Observed (i.e., not deconvolved from the PSF) component major axis, as derived from the *Chandra* X-ray data. Col. (5): Observed component minor axis, as derived from the *Chandra* X-ray data. Col. (6): Distance of component from the nucleus, as derived from the *Chandra* X-ray data. Cols. (7) and (8): Right ascension and declination, as derived from the *HST* image, after assuming the VLA position for the nucleus. Col. (9): The difference in right ascension in the sense optical − X-ray; thus a negative value in this column means that the X-ray component is closer to the nucleus than the optical. Col. (10): The difference in declination in the sense optical − X-ray. Col. (11): Notes connected with the astrometry. (a) Both the *HST* and *Chandra* data were registered to the VLA data assuming a common position for the nucleus of M87 in the radio, optical, and X-rays. The position given for the nucleus is therefore based on the absolute VLA astrometry, and all other positions are relative to it. (b) Optical position for knot HST-1 was based on fitting the unconvolved *HST* image with a Gaussian of FWHM 0.″174, which was taken as representative of the resolution of the *HST* data with this pixellation. The fit for the convolved *HST* image failed because of confusion with the nucleus. (c) Fits with a variable component size failed; a fixed FWHM of 1 ACIS pixel (0.″492) was assumed. (d) Component sizes based on a free component size, but component position is based on a fixed 0.″492 FWHM component to minimize error.

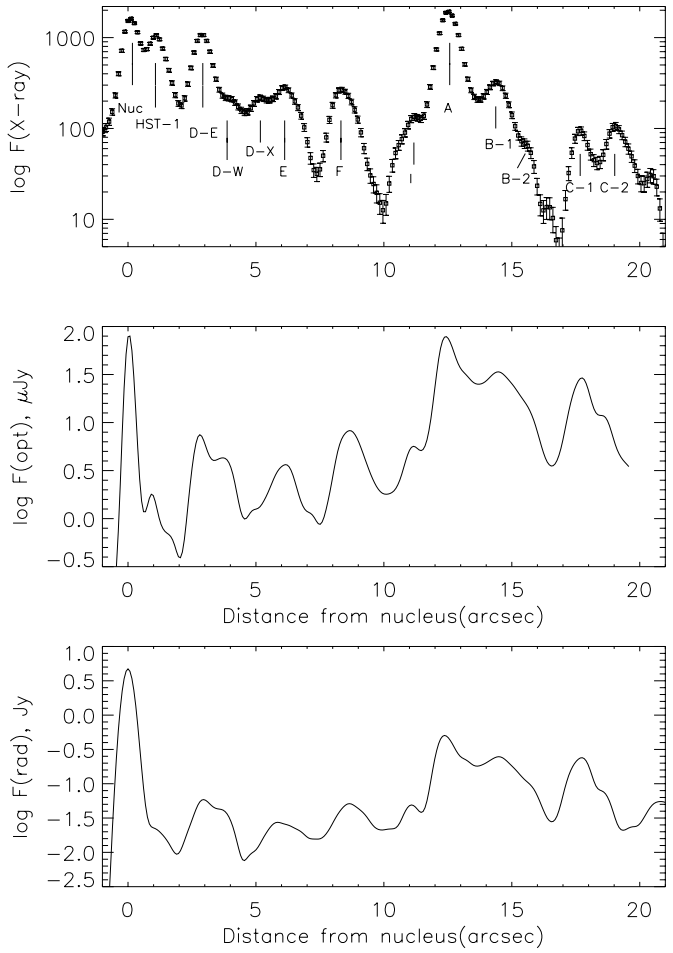

FIG. 3.—Runs of flux in the X-ray (0.3–1.5 keV band; *top*), optical (*HST* F814W; *middle*), and radio (VLA 15 GHz; *bottom*) bands. Flux in all three panels is plotted on a logarithmic scale. The optical and radio panels have been smoothed with 0.″4 Gaussians to match the resolution of the *Chandra* data. See § 3 for discussion.

measured in the optical and radio bands. Third, the loci of the flux maxima of each knot are not identical; i.e., there are real offsets between the X-ray and radio/optical component maxima in both the direction parallel to the jet (as found by M02 and WY02; see also below) and perpendicular to it.

Given that *Chandra*'s angular resolution is just sufficient to resolve the jet transverse to its axis downstream of knot A, it is best to compare the jet's radio, optical, and X-ray morphology in the context of runs of flux along the jet. We show these in Figure 3. As can be seen by examining these plots, the radio, optical, and X-ray flux track one another fairly closely in most regions of the jet. However, there do appear to be some differences in morphology. We have attempted to quantify these differences by fitting Gaussians at the location of each flux maximum to the (convolved) optical and (deconvolved) *Chandra* data sets, using the task `jmfit` in AIPS. The results are given in Table 1.

The data in Table 1 confirm that we resolve two jet components, namely knots A and B. However, they neither support nor reject the claims we make for knots C and I, as the surface brightnesses of those features are small enough that it was necessary to fix the size of the Gaussians used to fit them to obtain a good fit. Two other regions appear to have large Gaussian sizes as a result of this procedure, namely knots E and F. However, we cannot claim to have resolved these clearly, as we did not restrict the size of the Gaussians in the direction perpendicular to the jet, and moreover, as seen in Figure 2 their profiles are not conclusive as to whether the *Chandra* data resolve them. These same tests should be redone on knots E and F with summed *Chandra* data.

As can be seen in Table 1, most components do not have significantly different positions for their X-ray and optical flux maxima. There are, however, significant (>3 σ and >0.″1) optical–X-ray offsets for four components. These are knots D-W, D-X, F, and C-2. Two other knots, HST-1 and A, have offsets that are >3 σ but $\approx$0.″1. Because of the small sizes of these offsets (i.e., <0.2 times the angular resolution of the *Chandra* image), these offsets should be treated as less secure than larger offsets with identical statistical significance. The other knots have offsets in the range 1–3 σ that are not statistically significant. We deal with each of these in turn.

Knot HST-1 is the region of the jet where the fastest apparent superluminal motions have been seen ($\approx$6*c*; Biretta et al. 1999). It is also the location of a bright flare during 2000–2005 (Harris et al. 2003; Perlman et al. 2003), at which times the optical and X-ray flux maximum positions did coincide. M02 were also not able to find any optical–X-ray offsets; however, they did not apply deconvolution or pixel derandomization and therefore their reduction was not as sensitive to small offsets. Given the X-ray and optical flaring activity that is currently occurring in this region (Harris et al. 2003; Perlman et al. 2003; J. A. Biretta et al. 2005, in preparation) and that began in $\sim$1999 (i.e., between the *HST* and *Chandra* observations), we speculate that this possible optical–X-ray offset is a result of the flare.

Knots D-W and D-X are rather different cases. Knot D-W is not associated with a clear X-ray maximum, whereas there is a clearer optical maximum, as can be seen in both Figures 1 and 3. Knot D-X is in just the opposite situation: while there is a clear X-ray maximum at that location, there is not a clear optical maximum. In both cases it is therefore not surprising that we see some X-ray–optical offset. Our knowledge of the X-ray properties of these components would clearly benefit from deeper *Chandra* observations.

Knot F has two fairly clear optical maxima, which are separated by about 0.″4 in the *HST* images (see, e.g., P01a; Sparks et al. 1996); the optically brighter component is the one farther downstream. When the optical data are convolved to the resolution of *Chandra*, one cannot separate by eye these components. It is apparent that the X-ray maximum of knot F is associated with the upstream optical maximum. This observation agrees with WY02 (M02 did not have good enough statistics to comment on this region, as they discuss).

Our data suggest a small ($\sim$0.″1) but statistically significant (3.5 σ in R.A.; 5.5 σ in decl.) offset between the location of the optical and X-ray maxima of knot A. In this we agree with M02; we are also not in disagreement, however, with WY02, who note no offset to within $\pm$0.″1 but did not analyze *HST* data. The origin of this possible offset is not clear; however, it may have to do with the knot's double structure, as seen at 0.″1 resolution in the optical (P01a; Sparks et al. 1996). Indeed, a closer inspection of Figure 1 shows that the flux maximum region of knot A may be extended in the X-rays, along the length of the jet. This region would clearly benefit from improved angular resolution in the X-rays.

In the knot C region there also appear to be significant X-ray–optical differences, but the situation is somewhat complex. The X-ray and optical maxima of the region known in the optical as C-1 appear to coincide. However, knot C is a rather diffuse region in the optical, while in the X-rays there are two

TABLE 2
X-Ray Spectral Fits for Nucleus and Jet Knots

Component	Region (arcsec)	Distance (arcsec)	α_X	N_H (10^{20} cm^{-2})	K (10^{-5} photons s^{-1} keV^{-1})	S (1 keV) (μJy)	χ^2_ν
Nucleus	0.6 circle[a]	0	1.23 ± 0.11	3.5 ± 1.5	17.68	107	0.933/68
HST-1	0.6 circle[a]	1.25[b]	1.32 ± 0.08	2.4 ± 0.9	20.76	129	0.968/77
D-E	0.6 circle[a]	2.91	1.43 ± 0.09	2.4 (frozen)	8.31	51.5	0.745/34
E	2.4×1.6 box	5.80	1.48 ± 0.12	2.1 ± 1.1	5.04	32.2	0.618/64
F	2.4×1.6 box	7.75	1.64 ± 0.15	1.7 ± 1.3	3.70	20.1	0.760/42
A	2.3×2.0 box	12.6	1.61 ± 0.07	0.8 ± 0.5	27.7	156	1.198/89
B	3.3×1.8 box	15.35	1.59 ± 0.12	2.8 ± 1.2	5.70	30.3	0.678/58
C	7.8×1.5 box	20.9[c]	1.33 ± 0.06	2.4 (frozen)	3.58	20.6	1.576/49

[a] Radius of extraction circle.
[b] Offset by 0.″3 away from component centroid to avoid contamination from wings of nuclear PSF.
[c] Offset by 2″ away from nucleus in order to include any flux farther out in jet.

distinct maxima (Fig. 3). The second of these is close to the position of the optical component called C-2, but it is offset from the maximum of that component by about 0.″7. This was noticed also by M02 (who called the X-ray emission "G"; however, the optical component by that name is located farther from the nucleus) and WY02; however, neither of those teams gave a value for this offset. The α_{ox} map also shows that the downstream edge of knot C appears to have a smaller α_{ox} than regions farther upstream. This region would benefit from analysis of deeper *Chandra* observations.

Two other regions are also of note here. As can be seen in Table 1, our data suggest optical–X-ray offsets of nearly 3 σ significance at the flux maxima of knots E and D-E. The former was noted by WY02 but not M02; our data are suggestive of the same optical–X-ray offset (in the sense that the X-ray maximum is slightly upstream of its optical counterpart). These regions would clearly benefit from greater resolution in the X-rays, given that the possible offsets are $\sim$0.″1, only one-fifth of the *Chandra* pixel size.

3.2. *Optical to X-Ray, X-Ray, and Broadband Spectrum of the M87 Jet*

These data allow us to deduce new information regarding the X-ray and broadband spectrum of the M87 jet. M02 and WY02 published the first X-ray spectra of individual jet components. Those works established that the X-ray spectrum of each knot in the jet could be well described by a steep power law ($\alpha_X > 1$), although no information was included on knot HST-1 in either paper.

We have reanalyzed the X-ray spectrum of various components of the M87 jet, using regions similar to those in WY02, with the addition of a region for knot HST-1. Our analysis procedure included two differences from WY02. We made use of the latest available reduction procedures (see § 2.1), including the application of ACISABS. To extract the background spectrum, we used rectangles parallel to (north and south of) the jet to extract the background spectrum, a slightly different strategy from that used by WY02 or M02. We fitted single power law plus Galactic absorption models for all components, and in separate trials allowed first only α_X and then both α_X and N_H to vary. The full analysis was also done separately by each author, with E. S. P. using Sherpa and A. S. W. using XSPEC for spectral modeling. Data were generally fit in the 0.3–5 keV band. The results of these procedures are given in Table 2.

All knots are well described by single–power-law models; none requires a significant spectral break within the X-ray band. The variations in the power-law index of the jet's X-ray spectrum are small; in fact, all the knots appear consistent to within 2 σ with a power law of energy index $\alpha \sim 1.45$. There is, however, evidence for X-ray spectral variations along the jet. We find knot HST-1 to have an X-ray spectral index $\alpha_X \approx 1.3$, in agreement with WY02's estimate without deconvolution.

We reproduce to within the 90% confidence errors most of the values for α_X given in WY02 and M02 for which fits are given in those papers. We also find that the absorbing column densities are consistent with the Galactic value, $N_H(\mathrm{Gal}) = 2.4 \times 10^{20}$ cm^{-2}, with weak evidence that the column to the nucleus may exceed N_H(Gal). There are some areas of disagreement between our results and those of WY02, however. In particular, we do not unambiguously verify an absorbing column in excess of Galactic for the nucleus, as found by WY02, although both our analyses give a higher absorbing column for the nucleus than anywhere else. We also find that the photon indices of the knots given by WY02 are too small by, on average, 0.15–0.2, as noted in the erratum to WY02. Our testing reveals that the likely cause of these discrepancies is our correction of the ARF for the effects of absorption by contaminants on the surface of the CCD or its filter, using the program ACISABS. The existence of such absorption was not known when WY02 analyzed their data, with the results that their spectra for knots D, A, and B are too hard (by $\Delta\alpha \sim 0.2$–0.3) and their column density of the nucleus is overestimated. Thus the discussion by WY02 of the putative hard spectra of D, A, and B (their § 4.2) is not correct.

We also made a profile of α_X along the jet, by extracting photons in a 4″ wide strip and then dividing the regions so that each had approximately 800 counts. This procedure was done separately for both the 3.2 s frame time data set and for the 0.4 s frame time data set to allow for pileup in the bright regions. The fits were then done with N_H left constant given the information gleaned from the fits to individual knots. The run of α_X along the jet derived in this way is shown in the bottom panel of Figure 4. This map verifies the result above that all jet regions appear consistent to within 2 σ with a single–power-law shape. We do, however, find possible variations at the nearly 2 σ level, with somewhat flatter spectra interior to knot E, as well as in knot C, and steeper spectra in knots F, A, and B.

To investigate this issue further, we constructed images of two X-ray softness ratios $\mathrm{SR1} = F(0.3\text{–}1\ \mathrm{keV})/F(1\text{–}3\ \mathrm{keV})$ and $\mathrm{SR2} = F(1\text{–}3\ \mathrm{keV})/F(3\text{–}10\ \mathrm{keV})$. To increase the signal-to-noise ratio in the 3–10 keV band (which contains the smallest number of photons), we performed this calculation on the data binned to 0.″492 pixels, rather than 0.″123 pixels, and smoothed

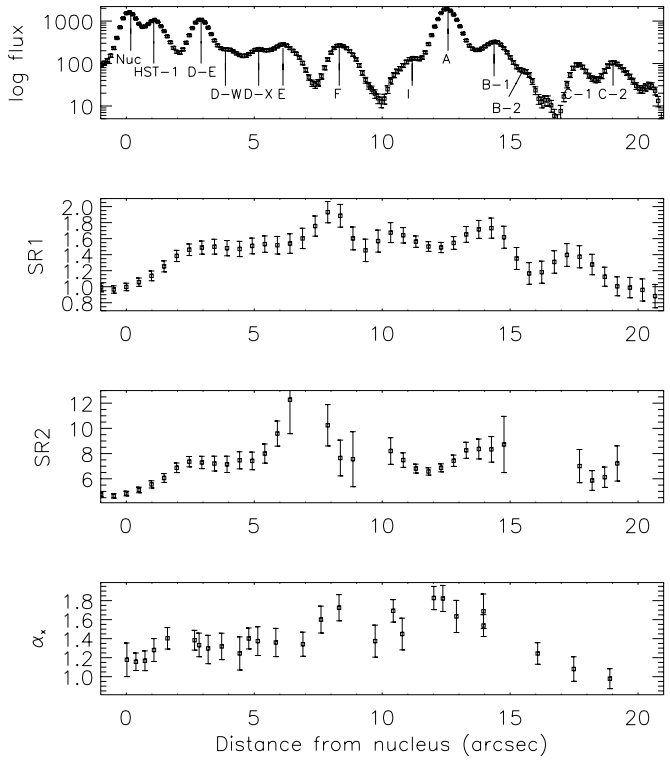

FIG. 4.—Runs of flux and X-ray spectral information along the jet. *Top*: Total X-ray flux. *Second*: X-ray softness ratio SR1 = $F(0.3-1\ \mathrm{keV})/F(1-3\ \mathrm{keV})$. *Third*: X-ray softness ratio SR2 = $F(1-3\ \mathrm{keV})/F(3-10\ \mathrm{keV})$. *Fourth*: X-ray spectral index α_X. Small variations are seen in the X-ray spectrum of the jet, with flatter spectra seen in the nucleus and knots HST-1, D, and C, and steeper spectra in knots F, A, and B. See § 3.2 for discussion.

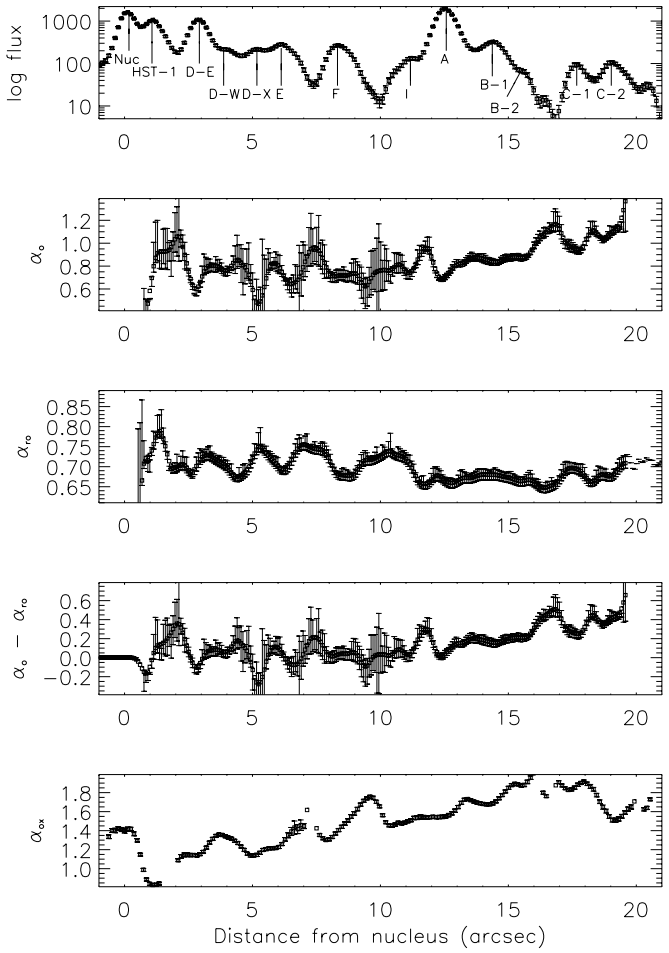

FIG. 5.—Run of X-ray flux compared to broadband spectral indices. *Top*: X-ray flux. *Second*: Optical spectral index α_o. *Third*: Radio–optical spectral index α_{ro}. *Fourth*: $\alpha_o - \alpha_{ro}$. *Fifth*: Optical–X-ray spectral index α_{ox}. Values of α_o, α_{ro}, and $\alpha_o - \alpha_{ro}$ are not shown within 0.″3 of the nucleus due to the saturation of the optical images at the position of the nucleus. The α_o, α_{ro}, and $\alpha_o - \alpha_{ro}$ runs have been smoothed with a Gaussian to a resolution of 0.″5. See §§ 3.2 and 4.1 for discussion.

the data with a Gaussian of $\sigma = 1$ pixel. We plot these ratios in Figure 4 (*middle panels*). As can be seen, the softness ratios are significantly smaller in the inner 3″ of the jet; i.e., the nucleus, HST-1, and possibly D-E have harder X-ray spectra than regions farther out. We also see evidence for some flattening of the X-ray spectrum in knot C, particularly in SR1. Thus, the 2 σ variations found in α_X (Fig. 4, *bottom panel*) are supported by the softness ratio analysis and are likely to be real.

A map of optical–to–X-ray spectral index α_{ox} is shown in the bottom panel of Figure 1. The run of α_{ox} along the jet is shown in Figure 5 compared to runs of α_o and α_{ro}. The α_{ox} map was made from the deconvolved, pileup-corrected 0.3–1.5 keV *Chandra* image and the F300W *HST* image from P01a, convolved to a resolution of 0.″5. Making the α_{ox} map required converting the *Chandra* image into units of μJy per pixel at 1 keV, which was done assuming a constant spectral index $\alpha_X = 1.4$ (see above) and the Galactic column density, $N_H(\mathrm{Gal}) = 2.4 \times 10^{20}\ \mathrm{cm}^{-2}$ (Biretta et al. 1991). The uncertainty in α_{ox} resulting from the assumption of constant α_X and N_H is tiny. The runs of α_o and α_{ro} are taken from P01a and smoothed to 0.″5 resolution.

As can be seen from Figures 4 and 5, α_{ox} varies considerably along the M87 jet. In knot HST-1, α_{ox} is considerably smaller than in any other region of the jet and is consistent with its large X-ray–to–optical ratio noted by M02 and WY02. The value of α_{ox} (HST-1) is 0.83, as compared to 1.45 for the nucleus and 1.2 for knot D. Note, however, that due to variability (see above), this value of α_{ox} may not be reliable. Beyond knot HST-1, there are two types of variation seen in α_{ox}. First, there is a steady spectral steepening, which begins at 2″ from the nucleus (the interknot region between knots HST-1 and D) and extends to 18″ from the nucleus (in knot C, between the two X-ray peaks). In this region α_{ox} increases from ≈1.2–1.4 at 2″–7″ from the nucleus (knots D and E) to ≈1.7–1.9 at 15″–18″ from the nucleus (knots B and C). Second, superposed on this steady increase are small but significant variations in the optical–to–X-ray spectrum at the positions of optical and X-ray flux maxima: at the positions of X-ray and optical maxima in the inner jet, α_{ox} decreases. These variations in α_{ox} appear largely to mirror the variations in ν_{break} determined by P01a through fitting the radio and optical spectra.

3.3. *Comparison of X-Ray Morphology with Optical Polarimetry*

A comparison between the morphology of the X-ray emission and maps of optical polarized flux and polarization position angle can give important information on the configuration of the magnetic field in the X-ray–emitting regions. This comparison is shown in Figure 6. The top panel of Figure 6 displays the X-ray flux (*gray scale*) with optical percentage polarization contours overplotted. In this panel, the data sets have been rotated so that the jet is along the *x*-axis, as in Figures 1–5. The lower three panels of Figure 6 show X-ray flux contours plotted

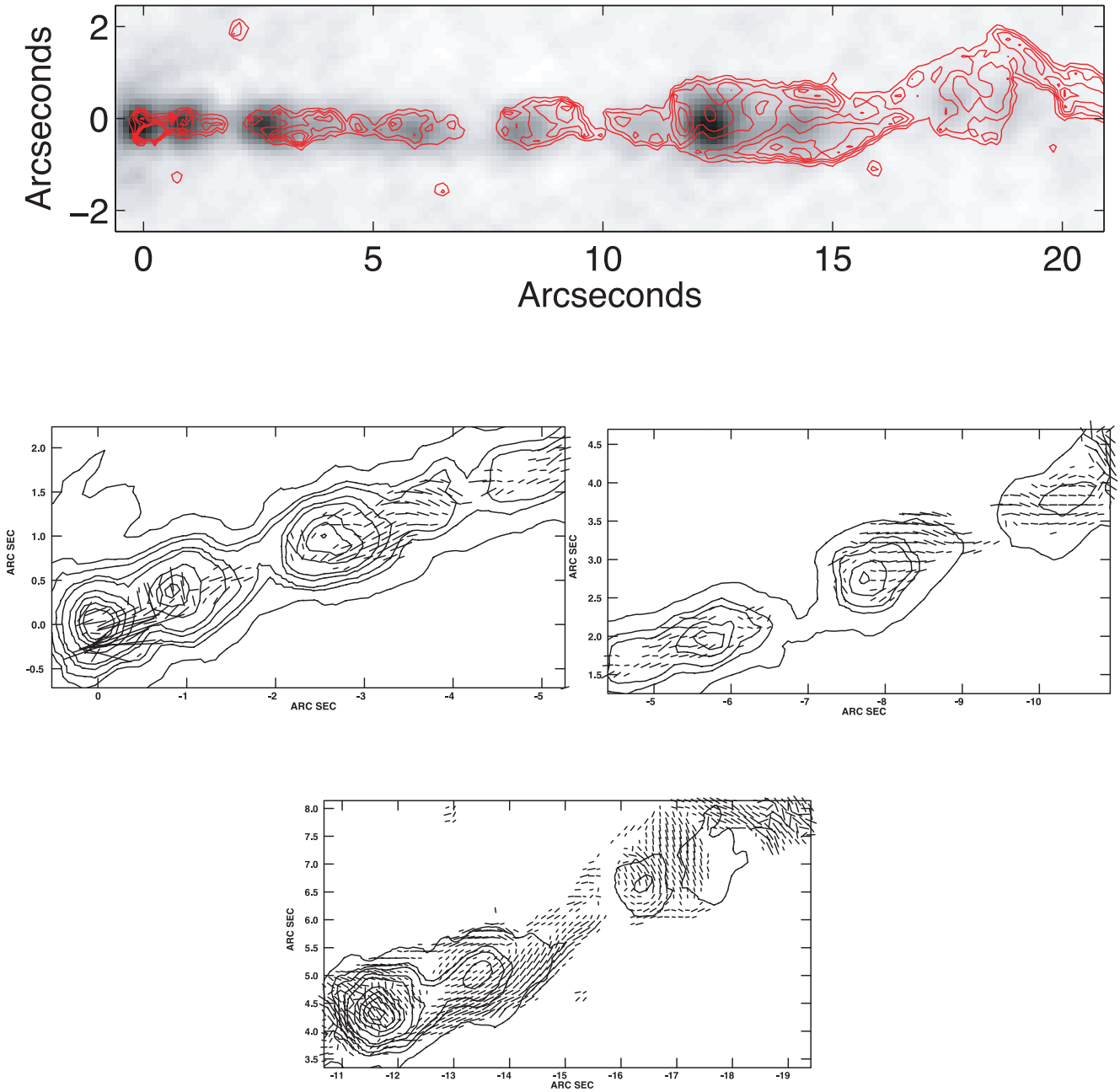

FIG. 6.—Plots comparing X-ray flux to optical polarization. At top, we show the *Chandra* 0.3–1.5 keV image in gray scale, with red contours representing the level of polarization in the optical (in percent). A logarithmic scale was used for the gray scale of the *Chandra* image, and contours are shown at 5, 15, 25, 35, 45, 55, and 65 percent polarization. The bottom three images show the X-ray flux in contours, with optical polarization (***B*** field) vectors overplotted. A vector 1″ long corresponds to 200% polarization. The optical polarization images shown here have not been smoothed with a 0.″5 Gaussian (unlike the total flux images discussed and shown previously), in order to bring out details in the magnetic field configuration of the jet. As can be seen, there is excellent agreement between the positions of X-ray flux maxima and optical polarization minima, particularly in the X-ray–brightest knots. See §§ 3.3 and 4.2 for discussion.

along with vectors whose direction is that of the magnetic field, as derived from the optical polarization measurements, and whose length is proportional to the optical percentage polarization. These panels are in the cardinal orientation (i.e., north up, east to the left). Each of the three lower panels shows a different region of the jet, with the region out to 5″ from the nucleus (knots HST-1, D-E, D-W, and D-X) shown in the left middle panel, the region between knot E and knot I (4.″5–11.″5 from the nucleus) shown in the right middle panel, and the outer jet (knot A and exterior to it, 11.″5–19″ from the nucleus) shown in the lower panel.

Figure 6 reveals a fairly consistent anticorrelation between optical percentage polarization and X-ray flux in the inner jet. In particular, the bright X-ray flux peaks are generally regions of low optical polarization, while peaks of optical polarization occur well away from the peaks of X-ray flux. A similar anticorrelation between optical flux and optical percentage polarization was noted in P99; however, as noted by those authors, there is no analogous anticorrelation between radio polarization and either radio or optical flux (their Figs. 3–7 and §§ 3–4).

It is interesting to elaborate on this anticorrelation. In three knot regions—HST-1, D-E, and D-X (Fig. 6, *top and left middle panels*)—the X-ray peak coincides exactly with the location of the optical polarization minimum, while in two other regions, the X-ray flux peak is either slightly upstream (knot E) or downstream (knot F) of the optical polarization minimum. As has

already been noted by P99, several of these optical polarization minima tend to be immediately downstream of regions of increased optical polarization, where the magnetic field is perpendicular to the jet. The morphology of the magnetic field is not the same for all the inner jet knots, however. For example, in knots HST-1, D-E, and F (Fig. 6, *middle panels*), large rotations of the magnetic field direction are seen just upstream of the X-ray flux maximum, while much less rotation is seen in knot E (Fig. 6, *right middle panel*), where the magnetic field appears to remain more closely parallel to the jet direction.

Three X-ray–bright knots in the inner jet are not strongly anticorrelated with optical polarization. The X-ray peaks of knots D-W and I (Fig. 6, *left middle and right middle panels, respectively*) correspond to regions of appreciable (15%–25%) but relatively constant optical polarization. Both show some rotation of the magnetic field direction, but again the details are different. In knot D-W the magnetic field becomes nearly perpendicular to the jet direction *downstream* (rather than upstream, as in knot D-E and others discussed above) of the flux maximum, while in knots D-X and I the orientation of the magnetic field seems unrelated to the jet direction.

The details of the relationship between X-ray flux and optical polarization appear significantly different in the outer jet (Fig. 6, *top and bottom panels*). Both the X-ray and optical flux peak of knot A, the brightest knot, occur well downstream of the peak in optical polarization noted by P99. The X-ray flux maximum is in a "valley" of reduced polarization between two high optical polarization regions (called HOP-1 and HOP-2 by P99) that surround both the X-ray and optical flux peaks. However, the optical polarization at the X-ray flux maximum is still considerable (≈35%). Moreover, as can be seen in Figure 6 (*bottom panel*), the magnetic field vectors in knot A are consistently perpendicular to the jet direction, a marked contrast to what is seen near flux peaks in the inner jet. Much lower optical polarizations (∼15%–20%) are seen in a band stretching for 0.″4 between the optical flux maxima of knots A and B. The X-ray flux peak of knot B, which coincides with optical knot B1, is different still: this knot is located in a region of fairly high optical polarization, with magnetic field vectors that tend to be parallel to the jet direction. Given the faintness of the regions between knots B1 and C in the X-rays, it is impossible to comment on the relationship between X-ray flux and optical polarization there. The X-ray flux peak corresponding to knot C1 occurs just downstream from an optical polarization minimum, in a region where the optical polarization is increasing with distance from the nucleus but has not yet reached maximum. However, the terminal X-ray flux peak corresponds to the region between optical knots C and G, and does correspond to a low optical polarization.

Comparing Figure 6 with Figures 1 and 3–5, two points can be made. First, the knots for which one sees a better correspondence between X-ray flux maxima and optical percentage polarization minima (e.g., knots HST-1, D-E, F, and A) tend to be brighter in the X-rays and have considerably smaller α_{ox} than the X-ray flux maxima that have weaker X-ray/optical polarization anticorrelations (compare Figs. 4, 5, and 6). The second point is that like the X-ray flux peaks, the optical percentage polarization minima tend to coincide with lower values of α_o and α_{ox}, and possibly larger α_{ro} values. In § 4 we analyze these features in the light of our spectral modeling.

4. PHYSICAL INTERPRETATION

Our reanalysis of the *Chandra* data confirms steep X-ray spectra ($\alpha_X > \alpha_r$) and is thus consistent with a synchrotron origin for the X-ray jet emission. However, here we have attempted a more thorough discussion of the M87 jet's morphology and broadband (particularly optical–to–X-ray) spectral energy distribution than previous authors. The correlation between X-ray emission and optical polarization is also discussed. The addition of these elements allows us to address the emission mechanism and physical conditions in more detail than was possible in previous papers.

4.1. *Synchrotron Emission Models and the Jet SED*

We have fitted synchrotron spectral models to each pixel of the radio through optical map cube described in § 3.1, using programs written by C. Carilli and J. P. Leahy (Carilli et al. 1991; Leahy 1991). The purpose of this exercise was not only to determine basic parameters such as synchrotron break frequency and injection index (an exercise that had already been carried out with the full-resolution optical data by P01a, who emphasize uncertainties in the determination of ν_{break}), but also to use the results of the fits to *predict* the X-ray flux and spectral index at various X-ray energies at each pixel for each model. We emphasize that the *Chandra* data were not used in the computation of these maps. In this way, we can determine the degree to which particle acceleration is or is not necessary at each position along the jet, and diagnose the loci and energy dependence of accelerated particles, where required. Only the smoothed radio–optical data were used for model fits.

The models we fitted to the data were as follows:

1. A Jaffe & Perola (1973) model (hereafter JP). In this model, a power-law spectrum with $n(E_e) \propto E_e^{-p}$ (E_e is the electron energy) is injected at $t = 0$ and allowed to evolve, taking into account losses to synchrotron radiation and/or inverse Compton scattering. There is continuous isotropization of the pitch-angle distribution of the electron population with time, but no further particle injection. The resulting spectrum is a power law at low energies with $\alpha = (p - 1)/2$, and an essentially exponential rollover above the synchrotron loss break frequency. In P01a, the JP model was still regarded as viable based only on simultaneous fitting of the entire radio–X-ray spectrum of the three knots that had been seen by *ROSAT* and *Einstein*. Our procedure rejects this model with very high confidence, as the exponential high-energy rollover underpredicts the X-ray flux at every pixel by many orders of magnitude and, moreover, its slope at X-ray energies is much larger than those observed. The JP model is therefore not mentioned further in this paper.

2. A Kardashev-Pacholczyk model (Kardashev 1962; Pacholczyk 1970; hereafter KP). This model assumes the same initial conditions as those in the JP model, but there is no pitch-angle scattering, so a high-energy "tail" of particles with small pitch angles develops. The resulting spectrum is a broken power law, with $\alpha = (p - 1)/2$ at low frequencies and $\alpha = (2p + 1)/3$ at high frequencies. The frequency of the break moves to lower values with increasing time. Since the spectral index of the radio knots (Biretta et al. 1991) is $\alpha_r \approx 0.6$, then $p = 2.2$. If $p_X = p_r$ (an assumption we return to below), then the KP model predicts X-ray spectral indices of $\alpha_X = 1.75$–1.9 for the integrated emission of a volume containing both sites of initial acceleration and regions into which the particles have moved; this range of values is somewhat larger than observed (Table 2; Fig. 4). Constancy of particle pitch angle is also somewhat implausible, in view of the likely scattering of relativistic particles by hydromagnetic waves (e.g., Wentzel 1977) and motion of particles into regions of different magnetic field direction. However, we retain this model in

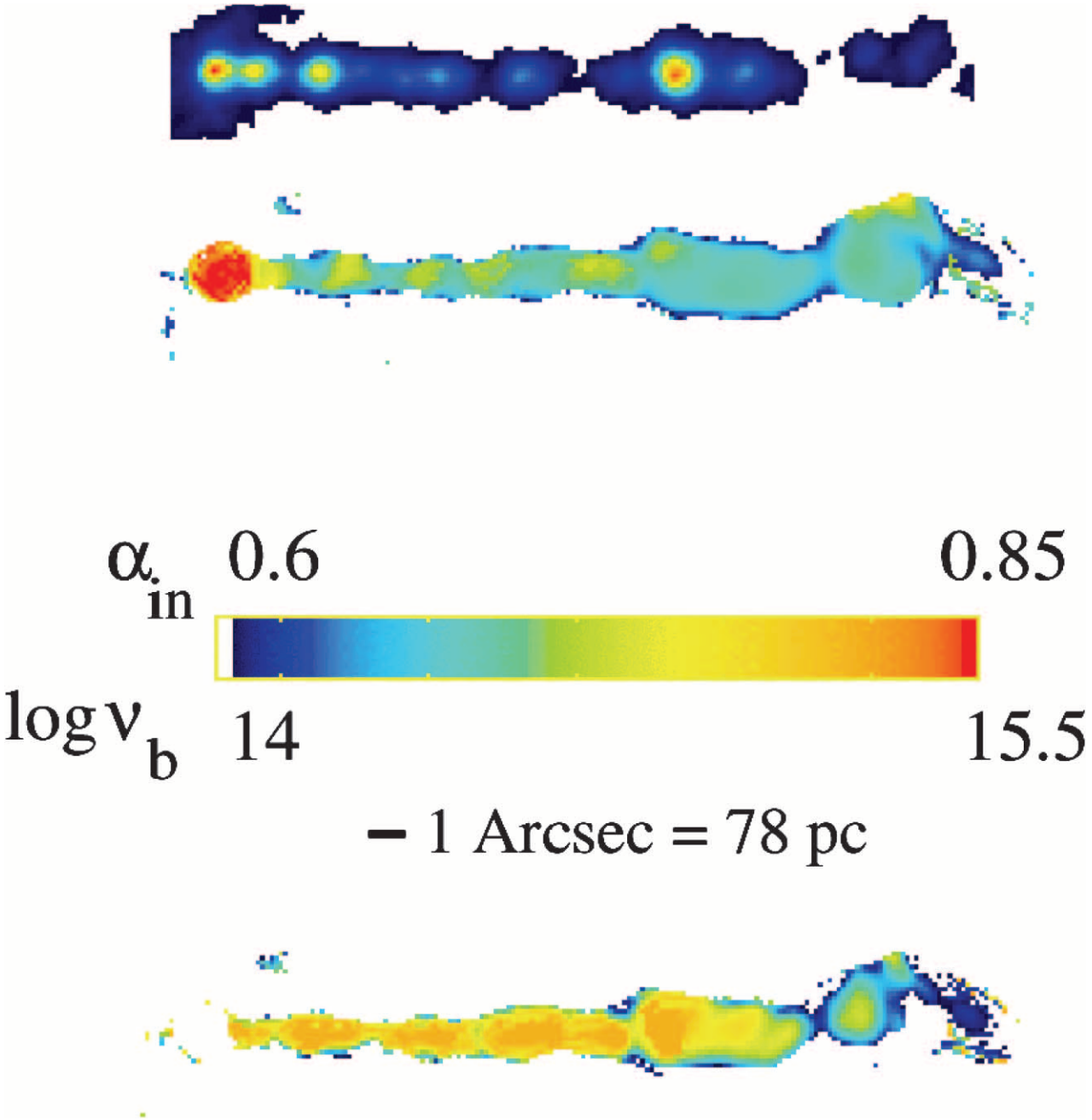

FIG. 7.—Results of modeling the radio–optical broadband spectrum with a CI synchrotron emission model in which the volume filling factor of regions of particle acceleration is energy-independent (so $\Delta\alpha = 0.5$). *Top*: Deconvolved X-ray image of the M87 jet, shown for reference. *Middle*: Injection index $\alpha_{\rm in}$, with the color scale running from 0.85 (*red*) to 0.6 (*blue*). *Bottom*: Synchrotron break frequency $\nu_{\rm break}$, with a color scale that runs from 10^{14} Hz (*blue*) to $10^{15.5}$ Hz (*red*). All data used for these maps have been smoothed with a 0.″5 Gaussian prior to modeling; full-resolution maps of these quantities have appeared previously in P01a. The trends shown in the KP model image of $\nu_{\rm break}$ are very similar, with essentially only a zero-point offset representing the overall differences in model characteristics (as described in Leahy 1991 and Carilli et al. 1991). The KP and CI models give identical $\alpha_{\rm in}$ images, as expected since that value is constrained by only the low-frequency spectral index. As shown, the X-ray flux maxima correspond well with regions of high $\nu_{\rm break}$, but there is no correlation between X-ray flux and $\alpha_{\rm in}$. See § 4.1 for discussion.

our discussion as it does not underpredict the fluxes by orders of magnitude (see below).

3. A "continuous injection" (hereafter CI) model (Kardashev 1962; Ginzburg & Syrovatskii 1968; Heavens & Meisenheimer 1987; Meisenheimer et al. 1989). In this case, a power-law distribution of relativistic particles is continuously injected at a constant rate. When the entire source is included in the telescope beam, there is a break of $\Delta\alpha = 0.5$ between the low- and high-frequency spectra, which are both power laws [$\alpha = (p - 1)/2$ at low frequencies and $\alpha = p/2$ at high frequencies]. If $p_{\rm X} = p_r$, we expect typical X-ray spectral indices $\alpha_{\rm X} \approx 1.1$, somewhat smaller than observed (Table 2; Fig. 4). P01a showed that such a CI model cannot apply to knots A, B, and D, since it overpredicts their X-ray fluxes by factors of 8–50. However, that result gave no indication of whether or not the CI model could apply with more complex assumptions about the sites, or spectrum, of accelerated particles.

We show in Figure 7 the results of a CI model fit, for the purpose of illustrating the trends in fitted break frequency $\nu_{\rm break}$

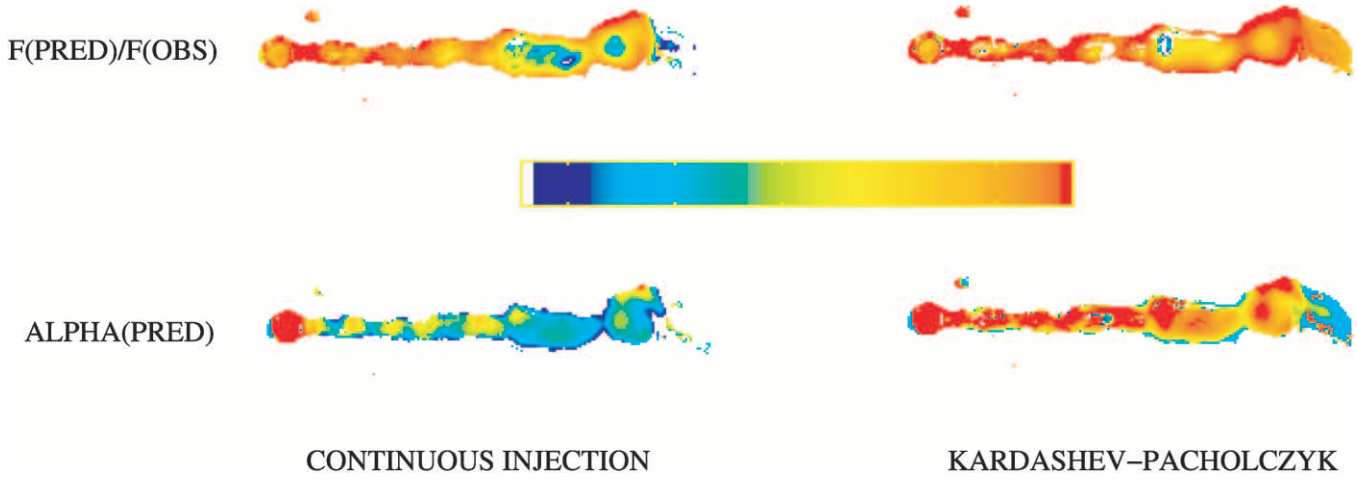

FIG. 8.—Distributions of the ratio $F_{\rm pred}/F_{\rm obs}$ and the predicted spectral index at X-ray frequencies for the CI (*left*) and KP (*right*) synchrotron models, with energy-independent filling factor $f_{\rm acc}$ for regions of particle acceleration. The top two panels show the ratio $F_{\rm pred}/F_{\rm obs}$ at 1 keV, with color scales that run from 1 (*red*) to 20 (*blue*) for the CI model and 0.01 (*red*) to 0.4 (*blue*) for the KP model. The bottom two panels show the predicted spectral index at frequencies $\nu \gg \nu_{\rm break}$ (computed at 1 keV), with color scales that run from 1.15 (*red*) to 1.25 (*blue*) for the CI model and 1.75 (*red*) to 1.9 (*blue*) for the KP model.

and injection index $\alpha_{\rm in}$. We stress that only the radio and optical data were used to develop this model. Note that the trends in $\nu_{\rm break}$ and $\alpha_{\rm in}$ are identical for the KP model, except for an offset in $\nu_{\rm break}$.

Two interesting things can be seen in Figure 7. First, the X-ray flux maxima correlate very well with the highest $\nu_{\rm break}$ regions of the M87 jet. Thus regions of high $\nu_{\rm break}$ are also anticorrelated with optical polarization. This indicates that the X-ray flux "knows about" $\nu_{\rm break}$; therefore, the X-ray–emitting particles cannot be an entirely independent population from those at lower energies. Instead, the correlation indicates that the X-ray emission is best explained as the high-energy extension of the radio–optical spectrum. Second, Figure 7 shows small variations in $\alpha_{\rm in}$. At some level, this is a feature induced by the data used in our modeling process, which included only a single radio point. This limitation forces $\alpha_{\rm in} \simeq \alpha_{\rm ro}$. We have not included a second radio point in the modeling because a radio spectral index map with sufficient resolution is not easily obtained; moreover, comparing the Biretta et al. (1991) values of α_r with our values of $\alpha_{\rm ro}$ reveals evidence of significant spectral curvature (typical $\Delta\alpha \approx 0.1-0.2$) between 15 GHz and the near-infrared point at 2.05 μm. We nevertheless assume an injection index $\alpha_{\rm in}$ equal to the local value of $\alpha_{\rm ro}$ at all energies in view of the small difference between α_r and $\alpha_{\rm ro}$.

We have used these spectral models to predict X-ray fluxes and spectral indices for the KP and CI models at several energies within the *Chandra* band: 0.3, 0.5, 1, 2, 3, 5, and 8 keV. This allows us to test the applicability of each synchrotron model to the M87 jet.

In Figure 8 we show the predictions at 1 keV for the CI (*left panels*) and KP (*right panels*) models. For each model, we show the ratio of predicted 1 keV flux to observed 1 keV flux (i.e., $F_{\rm pred}/F_{\rm obs}$; *upper panels*) and predicted spectral index at 1 keV (*lower panels*). The spectral indices are essentially $\alpha_{\rm X} = p/2$ (CI) or $\alpha_{\rm X} = (2p+1)/3$ (KP). The models shown in Figure 8 are for the case in which we adopted $\alpha_{\rm in}$ values from fitting the radio–optical data (see above), and thus approximate very closely the values of $\alpha_{\rm ro}$.

As can be seen, the KP model yields values of $F_{\rm pred}/F_{\rm obs}$ generally running between 0.10–1 in knot regions and 0.01–0.1 outside of knots. Further, as noted above, the KP model does not predict the correct X-ray spectral indices: $\alpha_{\rm X}$ is predicted to be 1.75–1.9, compared to the observed values of 1.3–1.6. Thus, by 10 keV the model underpredicts the observed X-ray fluxes by factors of 3–500, while below 1 keV it overpredicts the observed X-ray fluxes in some knots.

The CI model, by comparison, tends to consistently overpredict the 1 keV fluxes (as originally noted by P01a). As shown in Figure 8, we see generally lower values of $F_{\rm pred}/F_{\rm obs}$ in the interknot regions (often only 1–3), and higher values in the knots (3–20). Higher values are seen in the region exterior to knot A than closer to the nucleus (this trend is also seen in the KP model). The CI model comes closer to the observed X-ray spectral indices than the KP model, predicting $\alpha_{\rm X} \sim 1.15-1.25$, somewhat smaller than the values we observe in most of the jet, although not much flatter than the values seen in the nucleus, HST-1, and D. We discuss below the possible reasons behind these differences.

4.2. *A Model for Particle Acceleration in the M87 Jet*

The previous section leaves us with an interesting dichotomy. Namely, throughout the jet, the CI model overpredicts the X-ray flux, while the KP model underpredicts it. A second aspect is that the KP model predicts too steep an X-ray spectrum throughout the jet, while the CI model predicts too flat a spectrum. We have already noted the physical implausibility of the KP model. Resolution of its problems in describing the observations would require injection of high-energy particles to increase the X-ray flux and flatten the X-ray spectrum, i.e., the addition to the model of continuous injection at X-ray–emitting energies. We thus feel that an appropriate approach is to modify the CI model in such a way as to remove the discrepancy with observations.

The proposed model is thus a modified CI model in which it is assumed that

1. the volume within which particle acceleration occurs is energy-dependent, being smaller for particles of higher energy;
2. the spectrum of the injected electrons is a power law $n(E_e) \propto E_e^{-p}$ below the cutoff implied by assumption 1; and
3. the value of p is independent of energy and position.

We note that other modifications of the CI model can be made to remove the disagreement with observations and briefly address such possibilities in § 4.4. In the following, we derive the energy dependence of the volume within which particles are

accelerated. For simplicity, we assume that electrons that emit optical synchrotron emission are accelerated throughout the jet, i.e., with unit filling factor $f_{\rm acc}$, even though in P99 we advanced a model of partial energy stratification to explain the differences between the optical and radio polarization morphology. We can then derive $f_{\rm acc}$ at higher energies from

$$f_{\rm acc}(E_\gamma, x, y, z) = \frac{F_{\rm obs}(E_\gamma, x, y, z)}{F_{\rm pred,CI}(E_\gamma, x, y, z)}, \quad (1)$$

where E_γ is the energy of the photon emitted by the electron.

We expect $f_{\rm acc}$ to be a function of both position (as $F_{\rm pred}/F_{\rm obs}$ is observed to be; Fig. 8) and energy. Since, as shown in Figure 2, the *Chandra* observation barely resolves the jet's width, we feel it is most appropriate to explore the variations of $f_{\rm acc}(E_\gamma)$ as a function of distance from the nucleus along the jet. We show this in Figure 9 (*top*), which shows $f_{\rm acc}(r)$ at six different energies: $E_\gamma = 0.3$, 1, 2, 3, 5 and 8 keV.

Figure 9 (*top*) shows that at each energy $f_{\rm acc}$ varies quite widely. We first discuss its variations as a function of position, focusing on the 1 keV curve. These spatial variations of $f_{\rm acc}$ at any given energy are highly significant, with $f_{\rm acc}$ generally declining with increasing distance from the nucleus. Overall, in the inner jet one sees at 1 keV values of $f_{\rm acc} = 1-0.2$; i.e., particle acceleration is taking place in 100% (in knots D and E) to 20% (in knot I) of the jet volume. By comparison, in the outer jet we see values of $f_{\rm acc}(1\ {\rm keV}) = 0.2-0.07$; i.e., particle acceleration is taking place over 20% (in knot A) to 7% (in knot C) of the jet volume. Thus, in general, particle acceleration seems to be taking place in a larger fraction of the jet volume in the inner jet than in the outer jet.

Superposed on this general trend we also see variations on smaller angular scales. Not including the nucleus and HST-1, for which the values are unreliable due to variability, the highest value of $f_{\rm acc}$ is seen at D-X. In the inner jet, local minima in $f_{\rm acc}$ appear close to the locations of some of the knot flux maxima—in particular, knot D-E at $r = 2\farcs8$ and knot D-W at $r = 3\farcs8$; however, there is no clear pattern to these variations.

One also notices in Figure 9 (*top*) an obvious energy dependence of $f_{\rm acc}$, in the sense that particle acceleration regions occupy a smaller fraction of jet volume at higher energies. This seems to persist in all regions of the jet (once again, the variations in energy at the positions of the nucleus and HST-1 are not reliable due to variability). As can be seen, the variation is quite large: at any given position in the jet, $f_{\rm acc}$ varies by factors of 3–20 from the lowest (0.3 keV) to the highest (8 keV) energy. One simple parameterization of this energy dependence is a power law:

$$f_{\rm acc}(E_\gamma) \propto E_\gamma^{\xi} \propto E_e^{\xi/2}. \quad (2)$$

This parameterization allows one to relate ξ to the parameters in the synchrotron spectrum if the CI model holds. In particular, since the CI model predicts $F_{\nu,\rm pred} = K_p \nu^{-p/2}$ (for an energy-independent $f_{\rm acc}$) and we observe $F_{\nu,\rm obs} = K_{\rm obs}\nu^{-\alpha_{\rm X}}$ (where K_p and $K_{\rm obs}$ are constants), we have

$$f_{\rm acc} = F_{\nu,\rm obs}/F_{\nu,\rm pred} = {\rm constant} \times \nu^{-(\alpha_{\rm X}-p/2)}, \quad (3)$$

$$\therefore \xi = (-\alpha_{\rm X} + p/2) = (-\alpha_{\rm X} + \alpha_{\rm in} + 0.5). \quad (4)$$

We have calculated the value of ξ for different locations along the jet using equation (4). The values thus obtained are in approximate agreement with those found by fitting a power law to the energy dependence of f (Fig. 9, *top*). Figure 9 (*bottom*) shows that in the inner jet, $\xi = -0.4 \pm 0.2$. This small amount of variation is interesting, particularly given how much $f_{\rm acc}$ varies along the jet. More negative values ($\xi = -0.6$ to -0.8) are seen in two relatively isolated locations, $3''$ and $8''$–$9''$ from the nucleus. We also see $\xi = -0.7 \pm 0.2$ in knots A and B, $12''$–$15''$ from the nucleus. If one compares the top and bottom panels of Figure 9, one notices a possible correspondence between the first two of these regions, where we see the most negative exponents ξ and small local values of $f_{\rm acc}$ at low X-ray energies, suggesting that the decline in $f_{\rm acc}$ toward higher X-ray energies represents a continuation of a decline in $f_{\rm acc}$ from optical to X-ray energies. A recent analysis of deep UV imaging of the M87 jet with *HST* (Waters & Zepf 2005) found evidence that CI models with $f_{\rm acc} = 1$ fitted to the P01a radio–optical spectra exceed the observed flux at 1700 Å. This result is also qualitatively consistent with a decline in $f_{\rm acc}$ from optical to higher energies, but may more simply reflect uncertainty in fitting idealized models to fluxes measured at closely spaced wavelengths.

From the continuity of $f_{\rm acc}$ and ξ along the jet (Fig. 9) we are forced to conclude that particle injection and acceleration in the M87 jet must occur both within the knot regions and outside

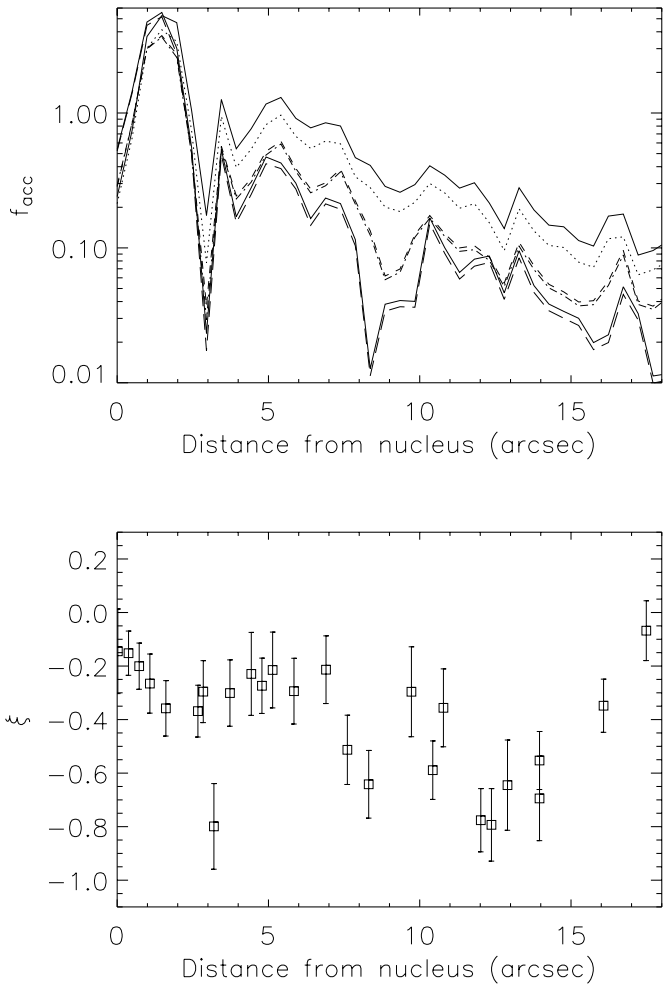

FIG. 9.—At top, we plot the filling factor $f_{\rm acc}$ of the regions within which particles radiating X-ray synchrotron radiation at E_γ are accelerated, vs. distance from the nucleus, for six different values of E_γ. From top to bottom, these are 0.3 keV (*solid line*), 1 keV (*dotted line*), 2 keV (*short-dashed line*), 3 keV (*dot-dashed line*), 5 keV (*triple-dot–dashed line*), and 8 keV (*long-dashed line*). The high values at $r = 0\farcs5-2''$ result from massive variability during 1999–2003 in knot HST-1 and should not be taken as representative of the knot at a single epoch. The general decrease in $f_{\rm acc}$ with increasing r is notable. At bottom, we plot the injection exponent ξ [$f_{\rm acc}(E) \propto E^{\xi}$] vs. distance from the nucleus, computed using eq. (4). See § 4.3 for discussion.

them. Jester et al. (2001, 2002) came to a similar conclusion for the 3C 273 jet based solely on radio–optical data.

4.3. *Sites and Types of Particle Acceleration*

The previous analysis established that in order to sustain the X-ray emission in the M87 jet, in situ particle acceleration almost certainly occurs, both within knots and outside them. Yet if the X-ray emission can be represented by the CI model, the volume within which X-ray–emitting particles are accelerated cannot fill the entire jet volume at any location, but instead fills only a fraction $f_{\rm acc}$ that varies with both position and energy.

As already noted in § 3.3, there is a strong correlation between the locations of optical polarization minima and X-ray flux maxima in several regions; this correlation is seen in knots HST-1, D-E, D-X, F, and possibly A and C1. Figure 6 shows that some of the regions in the inner jet (i.e., HST-1, D-E, D-X, and F) show increased optical percentage polarization and perpendicular magnetic field just upstream (by 0.″1–0.″3) of the X-ray peaks, low optical percentage polarization at the X-ray flux maxima, and then an increase of the optical percentage polarization immediately downstream of the X-ray peak. Often the downstream magnetic field direction is parallel to the jet. Knot A is similar, but here the downstream field is perpendicular to the jet. Ongoing *HST* polarimetry of the jets of several other nearby radio galaxies (E. S. Perlman et al. 2005, in preparation) shows that this trend of low optical polarization at X-ray flux maxima, often accompanied by changes in the polarization P.A., seems to persist in the population of X-ray synchrotron emitting jets as a whole.

Particle acceleration at shocks (e.g., Blandford & Ostriker 1978) through the first-order Fermi process is generally believed to occur in jets. For ultrarelativistic shocks, this model predicts an injection index of $p = 2.23$ (Kirk 2001; Kirk & Dendy 2001), in very good agreement with our analysis of these data. Further, the low observed polarization at X-ray peaks would result from beam averaging over the pre- and postshock regions, since the field direction is expected to be different in these two regions. The perpendicular field upstream of the knots might result from a second, transverse upstream shock. Alternatively, changes in polarization direction may result from differing contributions from a perpendicular field region in the center of the jet and a parallel field in the sheath (e.g., P99).

Our model implies that the volume within which particles are accelerated decreases with increasing particle energy. In other words, there is an upper cutoff to the energy of accelerated particles in any given element of volume. In the context of the first-order Fermi process in nonrelativistic shock waves (e.g., in supernova remnants), an upper cutoff may occur if there are no waves (because of ion-neutral damping) ahead of the shock capable of reflecting particles above a certain energy; such particles are then not reflected back and forth across the shock, as is needed to gain energy (Drury et al. 1996). In the ultrarelativistic case, damping of such long-wavelength modes would probably only be important downstream of the shock (J. G. Kirk 2005, private communication). One also expects a high-energy cutoff at energies for which the acceleration timescale is equal to the cooling time to synchrotron or inverse Compton losses. It is thus plausible that a high-energy cutoff should be present, but details are beyond the scope of this paper.

4.4. *Alternative Models*

The model discussed in § 4.2 is not unique. We see at least three alternative possibilities and deal with each of these briefly in this subsection.

One possible alternative model is that the index of the electron energy spectrum at injection is larger at X-ray–emitting energies than at lower energies. To account for the typical X-ray spectral index $\alpha_{\rm X} \approx 1.4$ would require an index at injection of $p_{\rm X} = 2.8$, in contrast with $p_r \simeq p_{\rm ro} \simeq p_o = 2.2$ at lower energies. This is, of course, an ad hoc postulate, but no more ad hoc than our suggestion that the volume filling factor within which particles are accelerated, $f_{\rm acc}$, declines with increasing energy at X-ray energies. These two pictures are very similar in that they represent simple phenomenological ways of modifying the classical CI model to allow agreement with the observations. However, we prefer our model in which $f_{\rm acc}$ declines with increasing energy for two reasons. First, the index at injection is $p = 2.2$ at all energies and all locations along the jet, consistent with current theoretical results for ultrarelativistic shocks (Kirk & Dendy 2001; Kirk 2001). Second, in the model in which the electron energy spectrum at injection is steeper at X-ray–emitting energies than at lower energies, the value of $p_{\rm X}$ must vary along the jet because $\alpha_{\rm X}$ varies.

Another possible model is that the X-rays may come from a population of relativistic electrons different from those responsible for the optical emission. This could be related to the "stratified flow" proposed by P99. This model seems less likely to us because we do not observe $\alpha_{\rm X} < \alpha_{\rm ox}$ or $\alpha_{\rm ox} < \alpha_o$ in any region of the M87 jet (contrary to the analysis of WY02; see § 3.2 and also the erratum of WY02). Jester et al. (2002) have suggested a model of this type for some regions of the 3C 273 jet; however, those 3C 273 jet components *do show* definite spectral hardenings in the ultraviolet, unlike M87.

Finally, within the classical CI model, it is possible for $\alpha_{\rm X} - \alpha_r$ to equal some value other than 0.5. Such can occur in relativistic electron diffusion loss models that allow the magnetic field and diffusion coefficient to vary as a function of distance from the location where the electrons are injected and that also allow the diffusion coefficient to be energy-dependent (Wilson 1975). Also, Coleman & Bicknell (1988) investigated models in which relativistic particles are accelerated in adiabatic, nonrelativistic bow shocks, and the electron distribution function evolves downstream through both adiabatic and radiative (synchrotron) losses. They too found breaks larger than 0.5. Unfortunately, little is known about particle propagation and magnetic field variations within the M87 jet, so models of this type are beyond the scope of this paper.

5. SUMMARY

We have performed a reanalysis of the deep *Chandra* image of the M87 jet, first analyzed by WY02. This analysis improves on that of WY02 in several respects, including an improved instrumental calibration as well as image deconvolution. The former has allowed us to obtain more reliable X-ray spectra along the jet, while the latter allowed us to improve the spatial resolution by nearly 50% and fully separate knots HST-1 and I from adjacent emission for the first time. There is evidence for slight spectral variations $\Delta\alpha \sim 0.3$ along the jet, with the flattest spectra ($\alpha_{\rm X} = 1.3$) observed in knots HST-1, D, and C and somewhat steeper spectra ($\alpha_{\rm X} = 1.6$) in knots F, A, and B. A careful comparison of the *Chandra* data to the multiwaveband *HST* imaging and polarimetry data of P99 and P01a has been performed in order to analyze the broadband spectrum of the jet and diagnose loci and mechanisms of particle acceleration.

In situ particle acceleration almost certainly occurs within the M87 jet. This has been demonstrated not only from particle lifetime arguments but also from spectral fits to the broadband spectra. We have used the absolute fluxes and spectra throughout

the X-ray band to determine the volume filling factor $f_{\rm acc}$ of regions within which particles are accelerated in the M87 jet. A continuous injection (CI) model in which both $f_{\rm acc}$ and the power-law index of the energy spectrum of the injected electrons are constant and independent of energy predicts $\Delta\alpha = 0.5$, where $\Delta\alpha$ is the change in spectral index between radio (or radio to optical) and X-ray frequencies. In contrast, we observe $\Delta\alpha = 0.7-1.0$, in agreement with the conclusion that a CI model with $f_{\rm acc} = 1$ overpredicts the X-ray emission by large factors (P01a; M02; WY02). To account for this larger $\Delta\alpha$, we have developed a model in which the filling factor $f_{\rm acc}$ varies as a function of position and energy from $\sim$1.0 to 0.01 at 1 keV, with a general decline as a function of both increasing distance from the core and increasing particle energy. Describing the energy dependence of the filling factor by $f_{\rm acc}(E_\gamma) \propto E_\gamma^{\xi} \propto E_e^{\xi/2}$ (where E_γ is the photon energy and E_e is the energy of the radiating electron), we find $\xi = -0.4 \pm 0.2$ in most of the inner jet and $\xi = -0.7 \pm 0.2$ for knots A and B. In this model, the index p of the relativistic electron energy spectrum at injection is $p = 2.2$ at all energies and locations, in excellent agreement with the predictions of models of cosmic-ray acceleration by ultrarelativistic shocks.

The X-ray peaks in the jet often coincide with minima in the optical percentage polarization, i.e., regions where the magnetic field is not ordered. We have suggested that this effect results from shock waves at the X-ray peaks. The shocks both accelerate X-ray–emitting electrons and reorient the field, resulting in low polarization through beam averaging. A tendency for the field to align perpendicular to the jet upstream of the X-ray peaks may reflect a second, transverse shock.

The need for high-energy particle acceleration (X-ray emission requires $\gamma \sim 10^7-10^8$) in the M87 jet is confirmed by the *Chandra* data; however, significant uncertainties remain, which would be alleviated by deeper, higher resolution X-ray data. A longer integration would determine the variations in X-ray spectral index with greater accuracy. We intend to revisit this issue in a future paper by adding together the multiple *Chandra* observations of M87 (C. C. Cheung et al. 2005, in preparation), which by now amount to well over 200 ks. The case for better resolution is equally clear: we do not resolve the inner jet well in the transverse direction, although we do resolve knots A, B, and C in the transverse direction. Observations with higher angular resolution would allow us to better pin down the relationship between X-ray flux, spectral index, and optical properties, as well as offsets between component maxima in different bands.

We wish to thank M. Karovska, A. Siemiginowska, D. P. Huenemoerder, and A. Ptak for ideas regarding the deconvolution of *Chandra* data. E. S. P. would like to thank D. Hudson and E. A. Tittley for help with analyzing *Chandra* data. We acknowledge J. A. Biretta, M. Birkinshaw, C. C. Cheung, D. E. Harris, M. Georganopoulos, S. Jester, J. G. Kirk, A. P. Marscher, C. P. O'Dea, W. B. Sparks, and D. M. Worrall for interesting conversations. We thank an anonymous referee for comments that improved this paper. E. S. P. acknowledges support from NASA under LTSA grant NAG5-9997, as well as *HST* grants STGO-7866.01, STGO-09142.01, STGO-09705.01, and STGO-09847.01 and *Chandra* grant SAO-03700786. A. S. W. thanks NASA for support under *Chandra* grants NAG-81027, NAG-81755, and G023147X and under LTSA grant NAG5-13065.

REFERENCES

Baade, W. 1956, ApJ, 123, 550
Biretta, J. A., & McMaster, M. 1997, WFPC2 Instrument Science Rep. 97-11
Biretta, J. A., Sparks, W. B., & Macchetto, F. D. 1999, ApJ, 520, 621
Biretta, J. A., Stern, C. P., & Harris, D. E. 1991, AJ, 101, 1632
Biretta, J. A., Zhou, F., & Owen, F. 1995, ApJ, 447, 582
Blandford, R. D., & Ostriker, J. P. 1978, ApJ, 221, L29
Carilli, C. L., Perley, R. A., Dreher, J. W., & Leahy, J. P. 1991, ApJ, 383, 554
Coleman, C. S., & Bicknell, G. V. 1988, MNRAS, 230, 497
De Young, D. S., Hogg, D. E., & Wilkes, C. T. 1979, ApJ, 228, 43
Drury, L. O'C., Duffy, P., & Kirk, J. G. 1996, A&A, 309, 1002
Feigelson, E. D., Schreier, E. J., Delvaille, J. P., Giacconi, R., Grindlay, J. E., & Lightman, A. P. 1981, ApJ, 251, 31
Ginzburg, V. L., & Syrovatskii, S. I. 1968, Ap&SS, 1, 442
Harris, D. E., Biretta, J. A., Junor, W., Perlman, E. S., Sparks, W. B., & Wilson, A. S. 2003, ApJ, 586, L41
Harris, D. E., & Stern, C. P. 1987, ApJ, 313, 136
Heavens, A., & Meisenheimer, K. 1987, MNRAS, 225, 335
Heinz, S., & Begelman, M. C. 1997, ApJ, 490, 653
Jaffe, W. J., & Perola, G. C. 1973, A&A, 26, 423
Jester, S., Röser, H.-J., Meisenheimer, K., & Perley, R. 2002, A&A, 385, L27
Jester, S., Röser, H.-J., Meisenheimer, K., Perley, R., & Conway, R. 2001, A&A, 373, 447
Kardashev, N. S. 1962, Soviet Astron.–AJ, 6, 317
Karovska, M., et al. 2001, in IAU Symp. 205, Galaxies and Their Constituents at the Highest Angular Resolutions, ed. R. T. Schilizzi (San Francisco: ASP), 66
Kirk, J. G. 2001, in ASP Conf. Ser. 250, Particles and Fields in Radio Galaxies, ed. R. A. Laing & K. M. Blundell (San Francisco: ASP), 41
Kirk, J. G., & Dendy, R. O. 2001, J. Phys. G, 27, 1589
Leahy, J. P. 1991, in Beams and Jets in Astrophysics, ed. P. A. Hughes (Cambridge: Cambridge Univ. Press), 100
Marshall, H. L., Miller, B. P., Davis, D. S., Perlman, E. S., Wise, M., Canizares, C. R., & Harris, D. E. 2002, ApJ, 564, 683 (M02)
Meisenheimer, K., Roeser, H.-J., Hiltner, P., Yates, M. G., Longair, M. S., Chini, R., & Perley, R. A. 1989, A&A, 219, 63
Meisenheimer, K., Roeser, H.-J., & Shlötelburg, M. 1996, A&A, 307, 61
Owen, F. N., Hardee, P. E., & Cornwell, T. J. 1989, ApJ, 340, 698
Pacholczyk, A. G. 1970, Radio Astrophysics (San Francisco: Freeman)
Perlman, E. S., Biretta, J. A., Sparks, W. B., Macchetto, F. D., & Leahy, J. P. 2001a, ApJ, 551, 206 (P01a)
Perlman, E. S., Biretta, J. A., Zhou, F., Sparks, W. B., & Macchetto, F. D. 1999, AJ, 117, 2185 (P99)
Perlman, E. S., Harris, D. E., Biretta, J. A., Sparks, W. B., & Macchetto, F. D. 2003, ApJ, 599, L65
Perlman, E. S., Sparks, W. B., Radomski, J., Packham, C., Fisher, R. S., Piña, R., & Biretta, J. A. 2001b, ApJ, 561, L51
Schmidt, G. D., Peterson, B. M., & Beaver, E. A. 1978, ApJ, 220, L31
Schreier, E. J., Burns, J. O., & Feigelson, E. D. 1981, ApJ, 251, 523
Schreier, E. J., Feigelson, E., Delvaille, J., Giacconi, R., Grindlay, J., Schwartz, D. A., & Fabian, A. C. 1979, ApJ, 234, L39
Sparks, W. B., Biretta, J. A., & Macchetto, F. 1996, ApJ, 473, 254
Tonry, J. L. 1991, ApJ, 373, L1
Waters, C. Z., & Zepf, S. E. 2005, ApJ, 624, 656
Wentzel, D. G. 1977, J. Geophys. Res., 82, 714
Wilson, A. S. 1975, A&A, 43, 1
Wilson, A. S., & Yang, Y. 2002, ApJ, 568, 133 (erratum 610, 624 [2004]) (WY02)
Zhou, F. 1998, Ph.D. thesis, New Mexico Institute of Mining and Technology